nature communications

Article

https://doi.org/10.1038/s41467-025-58654-0

Modulating the covalency of Ru-O bonds by dynamic reconstruction for efficient acidic oxygen evolution

Received: 25 August 2024

Accepted: 25 March 2025

Published online: 13 April 2025

Check for updates

Luqi Wang[1], Sung-Fu Hung[2], Sheng Zhao[1], Yue Wang[1], Suwan Bi[1], Shaoxiong Li[1], Jian-Jie Ma[2], Chenchen Zhang[3], Ying Zhang[3], Linlin Li[1] ✉, Tsung-Yi Chen[4], Han-Yi Chen[5], Feng Hu[1] ✉, Yuping Wu[6] & Shengjie Peng[1,6] ✉

Developing ruthenium-based oxide catalysts capable of suppressing lattice oxygen participation in the catalytic reaction process is crucial for maintaining stable oxygen evolution reaction (OER) under acidic conditions. Herein, we delicately construct a RuO_2 nanoparticle-anchored $LiCoO_2$ nanosheet electrocatalyst (RuO_2/$LiCoO_2$), achieving dynamic optimization of RuO_2 during the reaction process and improving catalytic stability. Benefiting from the unique electrochemical delithiation characteristics of the $LiCoO_2$ support, the covalency of the Ru-O bond is effectively regulated during the OER process. The weakened Ru-O covalent bond inhibits the participation of lattice oxygen in the catalytic reaction and ensures the continuous operation of the Ru active sites. Moreover, the extended Ru-O bond in the optimized RuO_2/$LiCoO_2$ catalyst reduces the formation energy barrier of the *OOH intermediates, accelerating the progress of the OER. As a result, the RuO_2/$LiCoO_2$ catalyst requires only an overpotential of 150 ± 2 mV at 10 mA cm^{-2} in 0.5 M H_2SO_4 and operates stably for 2000 h at 1 A cm^{-2} in a proton exchange membrane water electrolysis. This work opens new avenues for designing efficient ruthenium-based catalysts.

Proton exchange membrane water electrolysis (PEMWE) with high current density and low resistance loss is regarded as a promising hydrogen production technology in the future[1]. Currently, noble metal ruthenium (Ru) and iridium (Ir) oxide catalysts are extensively used in the anodes of PEMWE[2,3]. Compared to IrO_2, RuO_2 offers high activity and cost-effectiveness, presenting significant potential for application in acidic oxygen evolution reactions (OER)[4,5]. However, RuO_2 catalysts tend to follow the lattice oxygen mechanism (LOM) and generate numerous oxygen defects during the OER reaction, leading to crystal structure collapse[6,7]. Additionally, the metal Ru sites can be over-oxidized into soluble RuO_4 species, which separate from the crystal lattice under high oxidation potential, resulting in poor catalytic stability[8,9]. From a crystal structure perspective, the instability of RuO_2 is closely related to the charge distribution of the Ru-O bond[10–13]. Therefore, regulating the electronic state of the Ru-O bond to suppress the involvement of lattice oxygen in the OER process is an effective strategy for enhancing the activity and stability of RuO_2 catalysts.

Generally, electron-rich Ru sites in RuO_2 activate lattice oxygen and generate defects, while electron-deficient states tend to oxidize to excessively high valence states and dissolve[14,15]. Traditional electron-donating support strategies modulate the electron distribution of the

[1]College of Materials Science and Technology, Nanjing University of Aeronautics and Astronautics, Nanjing 210016, China. [2]Department of Applied Chemistry, National Yang Ming Chiao Tung University, Hsinchu, Taiwan. [3]Key Laboratory of Synthetic and Biological Colloids, Ministry of Education, School of Chemical and Material Engineering, Jiangnan University, Wuxi, Jiangsu 214122, China. [4]National Synchrotron Radiation Research Center, Hsinchu, Taiwan. [5]Department of Materials Science and Engineering, National Tsing Hua University, Hsinchu, Taiwan. [6]Confucius Energy Storage Lab, School of Energy and Environment & Z Energy Storage Center, Southeast University, Nanjing 211189, China. ✉e-mail: lilinlin@nuaa.edu.cn; fenghu@nuaa.edu.cn; pengshengjie@seu.edu.cn

Ru-O bond, preventing the dissolution of the metal center and following a relatively stable adsorption oxygen mechanism (AEM)[16,17]. At present, electron-donating supports with limited regulatory capacity cannot meet the demand for manipulating dynamically changing Ru-O bonds under complex high-potential OER conditions[18,19]. Therefore, designing supports capable of dynamically regulating the electronic structure of RuO_2 in response to changes in the catalytic reaction process is highly attractive. To address this challenge, transition metal oxides with cation intercalation dynamically optimize the local microenvironment of metal-oxygen bonds during the catalytic reaction through the extraction and insertion of cations[20,21]. Notably, lithium cobalt oxide ($LiCoO_2$) with a unique layered structure exhibits an ordered cation arrangement and superior thermodynamic stability[22–24]. The tight edge-shared CoO_6 octahedral structure in $LiCoO_2$ reduces the migration energy barrier of Li^+ and ensures two-dimensional diffusion of Li^+ in the plane, facilitating dynamic reconstruction during the catalytic process[25,26]. However, the multi-layered bulk structure of $LiCoO_2$ exhibits slow electron transport capability and limited surface area, which cannot meet the requirements for efficient catalyst support[25]. In this regard, two-dimensional $LiCoO_2$ nanosheets markedly shorten the intercrystalline electron transmission path and enhance conductivity[27]. Additionally, the two-dimensional nanosheet structure forms a fast electron transmission channel perpendicular to the exposure plane, resulting in strong metal-support interaction[28,29]. Therefore, using two-dimensional $LiCoO_2$ nanosheets as a support for RuO_2 is expected to achieve dynamic regulation of the electronic structure during catalytic reactions and exhibit high catalytic activity.

Herein, we propose an effective strategy to improve the charge distribution of RuO_2 through the unique dynamic evolution process of the $LiCoO_2$ support ($RuO_2/LiCoO_2$). The $LiCoO_2$ nanosheet support with electron-donating ability induces electron transfer from Co to Ru sites, providing electron compensation to stabilize the valence state of RuO_2. More importantly, the two-dimensional diffusion and extraction of Li ions within the interlayer of the $LiCoO_2$ nanosheet under OER potential cause the dynamic reconstruction and evolution of the $RuO_2/LiCoO_2$ catalyst interface. The unique dynamic self-optimization process moderately weakens the covalency of the Ru-O bond, suppressing the participation of lattice oxygen and achieving a good balance between catalytic activity and stability. The optimized Ru sites facilitate the formation of the *OOH intermediate, significantly lowering the catalytic energy barrier of the rate-determining step. Consequently, the $RuO_2/LiCoO_2$ electrocatalyst provides a current density of 10 mA cm^{-2} at an overpotential of 150 ± 2 mV and maintains stability for over 2300 h in 0.5 M H_2SO_4. In addition, $RuO_2/LiCoO_2$ as anode can operate continuously for 2000 h at 1 A cm^{-2} in a PEM electrolyzer. This work advances the application of ruthenium-based catalysts in PEMWE.

Results

Reaction mechanism and structural analysis

Due to the differences in the covalency of Ru-O bonds, Ru oxides follow either the lattice oxygen mechanism (LOM) or the adsorption oxygen mechanism (AEM) during the acidic OER process (Fig. 1a, b)[7,30]. In the LOM pathway, activated lattice oxygen with stronger covalency participates in the OER process, resulting in the generation of oxygen defects[31]. An excessive number of oxygen vacancies can induce detachment from the crystal lattice at the Ru metal sites, which greatly reduces the catalytic stability. However, Ru oxides with weak covalent Ru-O bonds follow the AEM mechanism, achieving a stable acidic OER process[13]. Therefore, dynamically regulating the covalency of Ru-O bonds during the catalytic reaction is crucial for enhancing catalyst stability. The O3-type $LiCoO_2$ material with Li element intercalation exhibits superior conductivity and structural stability. More importantly, the extraction of interlayer lithium ions at the OER potential triggers electron transfer, enabling real-time regulation of the covalency of metal-oxygen bonds (Fig. 1c). Additionally, we employ density functional theory (DFT) calculations to study the stability of different Co-based oxides in acidic environments. $LiCoO_2$ presents a thermodynamically unfavorable dissolution barrier, indicating that it can still maintain stability in an acidic environment (Fig. 1d). Inspired by these results, dynamically regulating the Ru-O bond covalency in RuO_2 using the layered $LiCoO_2$ support is expected to achieve high catalytic stability.

Materials characterization

A facile adsorption calcination strategy is employed to prepare $LiCoO_2$ nanosheets with loaded RuO_2 nanoparticles ($RuO_2/LiCoO_2$). Briefly, $LiCoO_2$ nanosheets are obtained through ultrasonic-assisted exfoliation of solid-phase synthesized bulk $LiCoO_2$ (Supplementary Figs. 1, 2). Subsequently, ruthenium ions are adsorbed on the $LiCoO_2$ surface through electrostatic binding and then calcined to form the $RuO_2/LiCoO_2$ electrocatalyst. According to the scanning electron microscopy (SEM) and transmission electron microscopy (TEM) images, $RuO_2/LiCoO_2$ exhibits an ultrathin nanosheet structure (Fig. 2a and Supplementary Figs. 3–5). Interestingly, the RuO_2 nanoparticles are tightly confined in the $LiCoO_2$ lattice in the high-resolution TEM (HRTEM) image, which is different from simple physical adsorption (Fig. 2b). A clear lattice contact exists between RuO_2 nanoparticles and the $LiCoO_2$ support, in which lattice stripes with interplanar spacings of 0.31 and 0.20 nm correspond to the RuO_2 (110) and $LiCoO_2$ (104) planes, respectively (Fig. 2c, h)[25]. The $LiCoO_2$ support provides lattice confinement for the RuO_2 nanoparticles to form a unique metal-support interaction. Atomic force microscopy (AFM) shows that the thickness of the $RuO_2/LiCoO_2$ nanosheet is 5.1 nm in Fig. 2d. The ultrathin nanosheet structure of $RuO_2/LiCoO_2$ maximizes the exposure of more Ru active sites. Atomic-resolution aberration-corrected high-angle annular dark-field scanning TEM (HAADF-STEM) is used to analyze the atomic structure of the $RuO_2/LiCoO_2$ composite. The Co atoms are arranged in an αβγ stacking mode in the HAADF-STEM image along the [010] zone axis, indicating the formation of O3-type $LiCoO_2$ and consistent with the XRD results (Fig. 2e and Supplementary Figs. 6, 7)[23]. The spacing of about 0.47 nm corresponds to the typical interlayer spacing of $LiCoO_2$. In addition, the bright Ru atomic array is embedded in the lattice of $LiCoO_2$ and exhibits superb lattice matching at the interface (Fig. 2f). The distribution of Ru, Co, and O elements in the energy dispersive spectroscopy (EDS) spectrum further confirms the uniformity of the heterostructure (Fig. 2g). The above analysis shows that the structurally ordered $LiCoO_2$ nanosheet support is closely connected to the RuO_2 nanoparticles, which provides the possibility for the optimization of the electronic structure.

To further understand the coordination structure and electronic states of $RuO_2/LiCoO_2$, X-ray absorption spectroscopy (XAS) was performed. As shown in Fig. 2i, the oxidation state of $RuO_2/LiCoO_2$ is lower than that of RuO_2 in the Ru K-edge X-ray absorption near-edge structure (XANES) spectra, implying the formation of an electron transfer channel between RuO_2 and $LiCoO_2$[32]. This is also consistent with the results of the first derivative of the Ru K-edge XANES spectra and high-resolution X-ray photoelectron spectroscopy (XPS) (Supplementary Figs. 8, 9). The $LiCoO_2$ nanosheet support with charge compensation effectively regulates the oxidation state of Ru sites, preventing excessive oxidation during the catalytic process. According to the Fourier transformed Ru K-edge extended X-ray absorption fine structure (FT-EXAFS) spectra, the Ru-O bond length is slightly shortened after contact between RuO_2 and $LiCoO_2$ (from 1.93 to 1.91 Å), which is attributed to the formation of interfacial interactions (Fig. 2j and Supplementary Figs. 10, 11 and Supplementary Tables 1, 2)[33]. The Co K-edge XANES of $RuO_2/LiCoO_2$ is transferred to higher energies compared to $LiCoO_2$ in Fig. 2k, which is consistent with the XPS valence band spectrum and

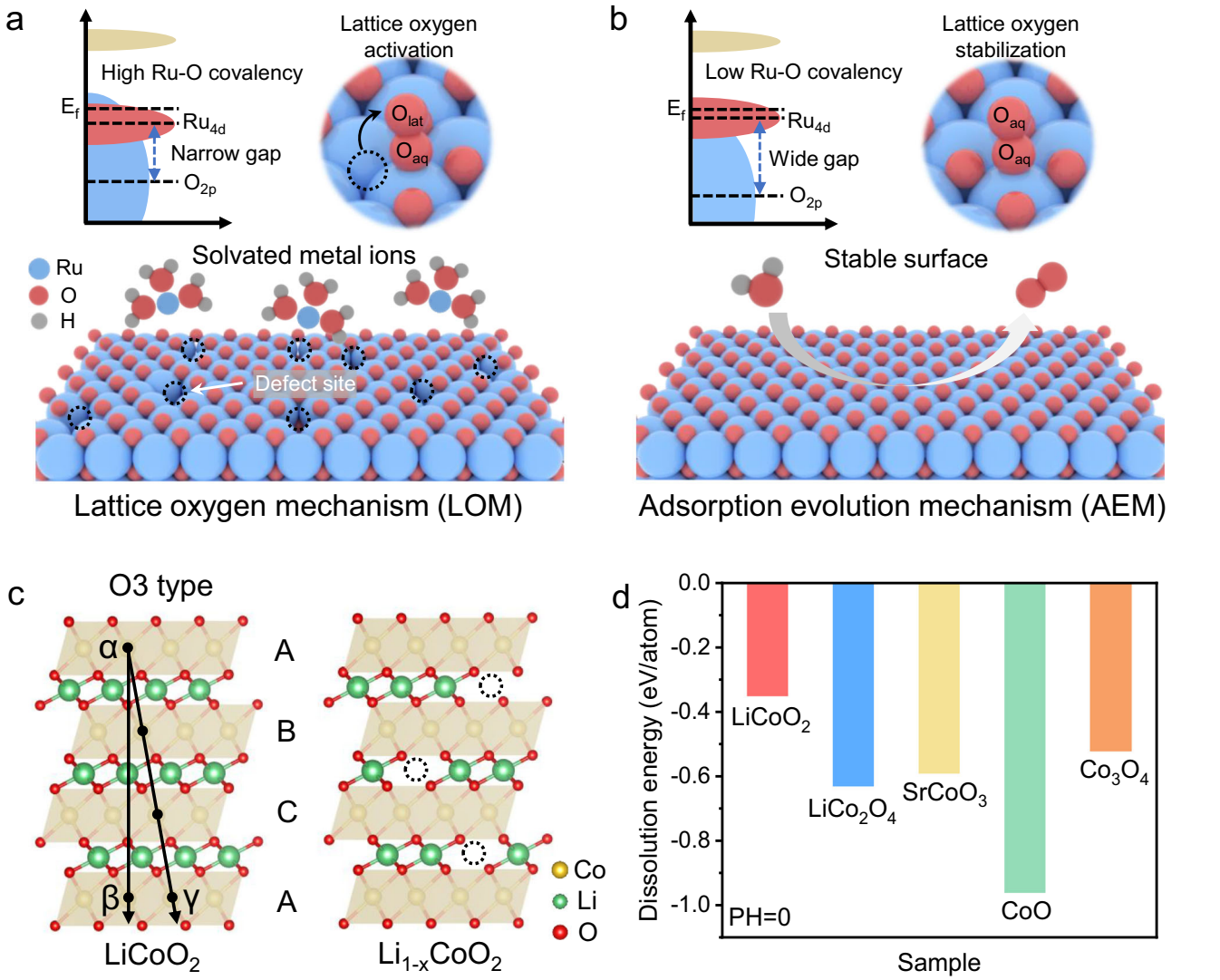

Fig. 1 | Schematic diagram of OER mechanism and structural analysis of lithium cobalt oxide. a LOM schematic of RuO_2 in acidic OER. **b** AEM schematic of RuO_2 in acidic OER. **c** Structural models of $LiCoO_2$ and $Li_{1-x}CoO_2$. **d** Dissolution energy barriers of cobalt-based oxides.

electron paramagnetic resonance (EPR) results. This verifies the electron-donating ability of the $LiCoO_2$ carrier (Supplementary Figs. 12, 13). Moreover, the main peaks of $RuO_2/LiCoO_2$ at 1.4 and 2.4 Å correspond to Co-O and Co-Co coordination shells in the Co K-edge FT-EXAFS spectra, respectively (Fig. 2l)[34,35]. It is worth noting that the Co-O bonds in $RuO_2/LiCoO_2$ are stretched more than $LiCoO_2$, which is consistent with the wavelet transform spectral results (Supplementary Figs. 14–16). The electron transfer from Co to Ru are verified by collecting electron energy loss spectra (EELS) of Co-$L_{2,3}$ and Ru-$M_{2,3}$ at the $RuO_2/LiCoO_2$ interface (Supplementary Fig. 17). Therefore, the interfacial interaction between RuO_2 and $LiCoO_2$ electronically compensates the Ru sites and improves the stability of the electrocatalyst.

OER electrocatalytic performance

Inspired by the structural advantages of the $RuO_2/LiCoO_2$ catalyst, the OER performance was evaluated via a three-electrode system in 0.5 M H_2SO_4. In Fig. 3a, the $RuO_2/LiCoO_2$ electrocatalyst exhibits an overpotential of 150 ± 2 mV at 10 mA cm^{-2}, which is much smaller than commercial RuO_2 (260 ± 4 mV) (denoted Com-RuO_2) and RuO_2 (210 ± 5 mV) (Supplementary Figs. 18–24). In comparison, the highly acidic OER activity of $RuO_2/LiCoO_2$ also surpasses most previously reported noble metal-based electrocatalysts (Supplementary Figs. 25 and Supplementary Table 3). The Tafel slope of $RuO_2/LiCoO_2$ (51.97 mV dec^{-1}) shows improved reaction kinetics compared to RuO_2 (62.06 mV dec^{-1}) and Com-RuO_2 (92.80 mV dec^{-1}) (Fig. 3b)[36]. At the OER potential, $RuO_2/LiCoO_2$ exhibits fast intermediate conversion efficiency. Meanwhile, the phase angle of $RuO_2/LiCoO_2$ rapidly decreases at different potentials in the Bode plot, further confirming the rapid charge diffusion on the catalyst surface (Supplementary Figs. 26–28 and Supplementary Table 4). The mass activity of the $RuO_2/LiCoO_2$ catalyst is 41.81 times that of RuO_2 at an overpotential of 240 mV in Fig. 3c. In addition, the turnover frequency (TOF) and OER current normalized by the electrochemically active surface area (ECSA) of $RuO_2/LiCoO_2$ electrocatalysts are significantly higher than RuO_2 (Supplementary Figs. 29–32 and Supplementary Table 5). The catalyst durability is tested using chronopotentiometry to evaluate the potential for practical applications. The $RuO_2/LiCoO_2$ electrocatalyst can operate stably for 2300 h at a current density of 10 mA cm^{-2}, while RuO_2 almost loses its activity after 400 h (Fig. 3d and Supplementary Fig. 33). The above results show that the $LiCoO_2$ support in the $RuO_2/LiCoO_2$ electrocatalyst avoids the dissolution of RuO_2 in acidic OER to achieve sustained acidic OER catalytic activity.

To evaluate the industrial application potential of $RuO_2/LiCoO_2$, a PEM electrolyzer was assembled with $RuO_2/LiCoO_2$ and

https://doi.org/10.1038/s41467-025-58654-0

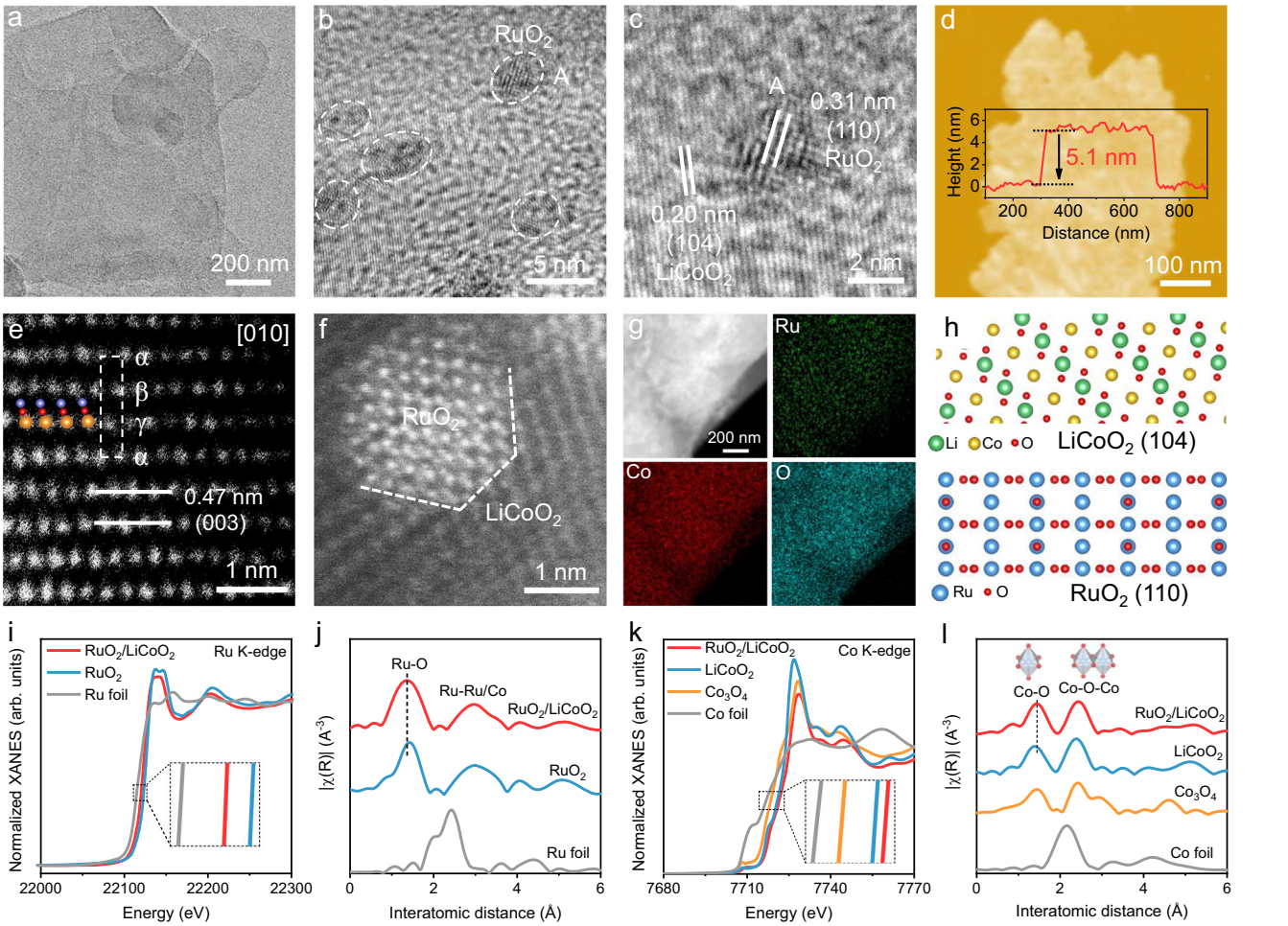

Fig. 2 | Characterizing the structure of $RuO_2/LiCoO_2$. **a** TEM, (**b**, **c**) HRTEM, and (**d**) AFM images of $RuO_2/LiCoO_2$ (inset: height profile of $RuO_2/LiCoO_2$). **e**, **f** HAADF-STEM images of $RuO_2/LiCoO_2$. **g** The EDS elemental mapping of $RuO_2/LiCoO_2$. **h** The atomic model of RuO_2 and $LiCoO_2$. **i** Normalized Ru K-edge XANES spectra and (**j**) Ru K-edge FT-EXAFS spectra of $RuO_2/LiCoO_2$, RuO_2, and Ru foil, respectively. **k** Normalized Co K-edge XANES spectra and (**l**) Co K-edge FT-EXAFS spectra of $RuO_2/LiCoO_2$, $LiCoO_2$, Co_3O_4, and Co foil, respectively.

Pt/C as anode and cathode catalysts, respectively. Specifically, $RuO_2/LiCoO_2$||Pt/C only requires a cell voltage of 1.68 V to reach a current density of 1 A cm^{-2}, which is significantly lower than RuO_2||Pt/C (1.84 V) (Fig. 3e). Overpotential analysis shows that improved mass transport alleviates concentration polarization effects in the local reaction environment, indirectly enhancing catalytic kinetics (Supplementary Fig. 34). Furthermore, the mass activity of $RuO_2/LiCoO_2$||Pt/C (2.56 A mg_{Ru}^{-1}) is approximately 21.33 times greater than that of RuO_2||Pt/C (0.12 A mg_{Ru}^{-1}) at a cell voltage of 1.7 V (Supplementary Fig. 35). The mass activity and cost of $RuO_2/LiCoO_2$||Pt/C are also much lower than those of commercial IrO_2||Pt/C (Supplementary Fig. 36). Strikingly, the PEM electrolyzer using $RuO_2/LiCoO_2$||Pt/C can operate stably for 2000 h at a current density of 1 A cm^{-2} with negligible decay in Fig. 3f, indicating the potential of the $RuO_2/LiCoO_2$ catalyst for practical applications. The long-term durability of $RuO_2/LiCoO_2$||Pt/C in PEMWE also exceeds that of most recently reported various high-performance electrocatalysts (Supplementary Table 6). These findings demonstrate that the $RuO_2/LiCoO_2$ electrocatalyst exhibits outstanding performance as a choice for hydrogen production in the PEM electrolyzer, providing strong support for sustainable energy production.

Structural transformation after stability

The physical structure of the $RuO_2/LiCoO_2$ electrocatalyst after OER stability testing was investigated to explore the influencing factors for the improved catalytic activity. SEM and TEM images show that RuO_2 nanoparticles remain tightly supported on the surface of $LiCoO_2$ nanosheets in the $RuO_2/LiCoO_2$ electrocatalyst after stability testing (Supplementary Figs. 37, 38). Besides, a reconstructed amorphous layer can be clearly observed on the surface of $LiCoO_2$ nanosheets in $RuO_2/LiCoO_2$. This layer is attributed to the migration and extraction of interlayer Li-ions during voltage application, resulting in the formation of a surface $Li_{1-x}CoO_2$ amorphous layer. Compared with the original $RuO_2/LiCoO_2$, the (003) crystal plane peak of $RuO_2/LiCoO_2$ after OER stability shifts to a lower angle, which may be attributed to the lattice distortion caused by the extraction of Li ions (Fig. 4a and Supplementary Fig. 39). Additionally, the Raman spectrum of $RuO_2/LiCoO_2$ detects two characteristic peaks of E_g and A_{1g} modes at 484 and 594 cm^{-1}, corresponding to O-Co-O bending and Co-O stretching, respectively (Fig. 4b and Supplementary Fig. 40). Due to the enhanced polarity of the Co-O bond induced by Li extraction, the E_g and A_{1g} characteristic peaks of $RuO_2/LiCoO_2$ exhibit a blue shift after OER stability (Supplementary Fig. 41)[23]. In particular, the new peak at 665 cm^{-1} after stabilization is attributed to the Co-O bonds of the spinel structure $Li_{1-x}CoO_2$ ($LiCo_2O_4$) of the surface reconstruction layer, which enhances the polarity of the Co-O bonds. The interlayer Li ions detach from $RuO_2/LiCoO_2$ through a two-dimensional diffusion path under the OER potential, performing dynamic structural reconstruction and altering the interface coordination environment of the catalyst.

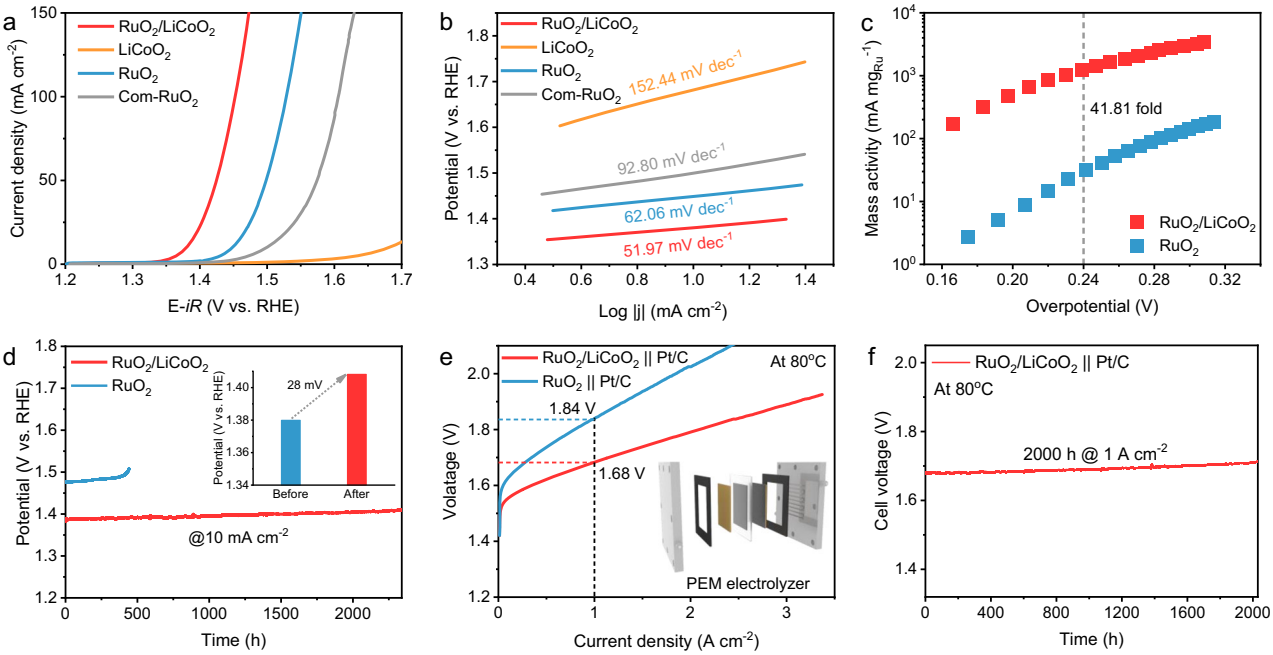

Fig. 3 | Electrocatalytic performance of $RuO_2/LiCoO_2$. **a** OER polarization curves and (**b**) Tafel plots of $RuO_2/LiCoO_2$, RuO_2, Com-RuO_2, and $LiCoO_2$ in 0.5 M H_2SO_4 electrolyte, respectively. The voltage is corrected by an automatic 90% of iR compensation (R is 1.10 ± 0.02 Ω). **c** Mass activity of Ru atoms in $RuO_2/LiCoO_2$ and RuO_2 as a function of overpotential. **d** Chronopotentiometric curves of $RuO_2/LiCoO_2$ and RuO_2 at 10 mA cm^{-2}, respectively (Inset: Potential changes of $RuO_2/LiCoO_2$ before and after stabilization). **e** The polarization curves of PEMWE with $RuO_2/LiCoO_2$ | |Pt/C and RuO_2 | |Pt/C catalyst in pure water at 80 °C without iR-correction. **f** Chronopotentiometric curve of PEMEW using $RuO_2/LiCoO_2$ | |Pt/C catalyst at 1 A cm^{-2}.

The electronic states of $RuO_2/LiCoO_2$ catalysts before and after OER stability are further analyzed to understand the influence of the reconstruction process. The Co^{3+} ratio of $RuO_2/LiCoO_2$ after OER stabilization increases compared with the pristine $RuO_2/LiCoO_2$, implying the reduction of electron density for Co sites (Fig. 4c and Supplementary Fig. 42)[37,38]. The dynamic extraction of Li ions induces electron transfer, leading to partial oxidation of Co sites and increased covalency in the Co-O bond. Additionally, the proportion of Ru^{4+} in $RuO_2/LiCoO_2$ slightly increases from 58.02% to 61.17% after the stability measurement[39]. As a comparison, the proportion of Ru^{4+} in RuO_2 after the stability measurement is 85.24%, which is much higher than that of $RuO_2/LiCoO_2$ (Supplementary Figs. 43, 44). Despite the slight oxidation of the $LiCoO_2$ support, it can maintain the oxidation state of RuO_2 by continuously donating electrons, thereby preventing the dissolution of Ru sites (Supplementary Figs. 45, 46). A structural model of $RuO_2/LiCoO_2$ after partial delithiation ($RuO_2/Li_{1-x}CoO_2$) is constructed to reveal the changes in electronic structure by DFT calculations (Supplementary Fig. 47). The Bader charge indicates that Ru in $RuO_2/LiCoO_2$ obtains about 0.169 e of electrons from the $LiCoO_2$ support (Fig. 4d)[40,41]. Due to the extraction of Li ions, the charge density at the Ru sites in $RuO_2/Li_{1-x}CoO_2$ (6.584 e) is lower than that of $RuO_2/LiCoO_2$ (6.626 e), while remaining higher than that of RuO_2 (6.457 e) (Fig. 4e). Crystal orbital Hamiltonian population (COHP) analysis shows that the Ru-O bond covalency of $RuO_2/Li_{1-x}CoO_2$ (−4.07 eV) is lower than that of $RuO_2/LiCoO_2$ (−4.35 eV) (Fig. 4f)[42,43]. The unique delithiation process ensures dynamic regulation of the covalency of the Ru-O bond during the catalytic process to suppress the participation of lattice oxygen (Fig. 4g).

In situ characterization of catalyst structural changes

In-situ XAS was implemented to explore the dynamic evolution mechanism of electrocatalysts in the OER process (Supplementary Fig. 48). In the fitted Ru K-edge FT-EXAFS spectra, the Ru-O bond of $RuO_2/LiCoO_2$ is appropriately extended as the potential increases from open circuit voltage (OCV) to 1.7 V (from 1.90 to 1.99 Å), indicating that the covalency of Ru-O is weakened (Fig. 5a, b and Supplementary Fig. 49 and Supplementary Table 7)[44]. In contrast, the Co-O bond tends to be more covalent during the delithiation process, resulting in a negative shift of the Co-O coordination shell in $RuO_2/LiCoO_2$ and the formation of a surface reconstruction layer (from 1.92 to 1.82 Å) (Supplementary Figs. 50, 51 and Supplementary Table 8)[45]. The wavelet transform of Ru K-edge and Co K-edge EXAFS spectra also intuitively confirm this result (Supplementary Figs. 52–54). Thus, the dynamic extraction of lithium ions regulates the covalency of the Ru-O bond through interfacial interactions, which can restrict the participation of lattice oxygen and maintain the structural stability of RuO_2 (Fig. 5c). Notably, the Ru-O bond in RuO_2 undergoes a significant shortening from 1.93 Å to 1.81 Å as the voltage transitions from OCV to 1.7 V (Fig. 5d, e and Supplementary Figs. 55–57 and Supplementary Table 9). The excessive enhancement of the covalency of the Ru-O bond provides conditions for triggering lattice oxygen to participate in the OER reaction[44]. Moreover, the slight change in the Ru-O coordination number in $RuO_2/LiCoO_2$ indicates the stability of the coordination structure of RuO_2. As a comparison, a reduced coordination number can be observed for the Ru-O bonds in RuO_2, which is attributed to the presence of defective oxygen (Fig. 5f). Due to the strong covalency of the Ru-O bond, RuO_2 follows the LOM path and generates a large number of oxygen defects during the OER process, leading to the collapse of the catalyst surface structure.

To elucidate the electronic structure changes of the electrocatalyst at high potentials, the oxidation states of $RuO_2/LiCoO_2$ and RuO_2 are detected by in situ XANES spectra. The average valence state of Ru species in $RuO_2/LiCoO_2$ rises gently from +3.82 to +4.21 as the potential transitions from OCV to 1.7 V vs. RHE in Fig. 5g (Supplementary Fig. 58). This further confirms that the strong electronic interaction between the $LiCoO_2$ and RuO_2 interface inhibits the excessive oxidation of RuO_2. In addition, the Co species in the $RuO_2/LiCoO_2$ catalyst can still maintain an oxidation state of +3.16 at a high

https://doi.org/10.1038/s41467-025-58654-0

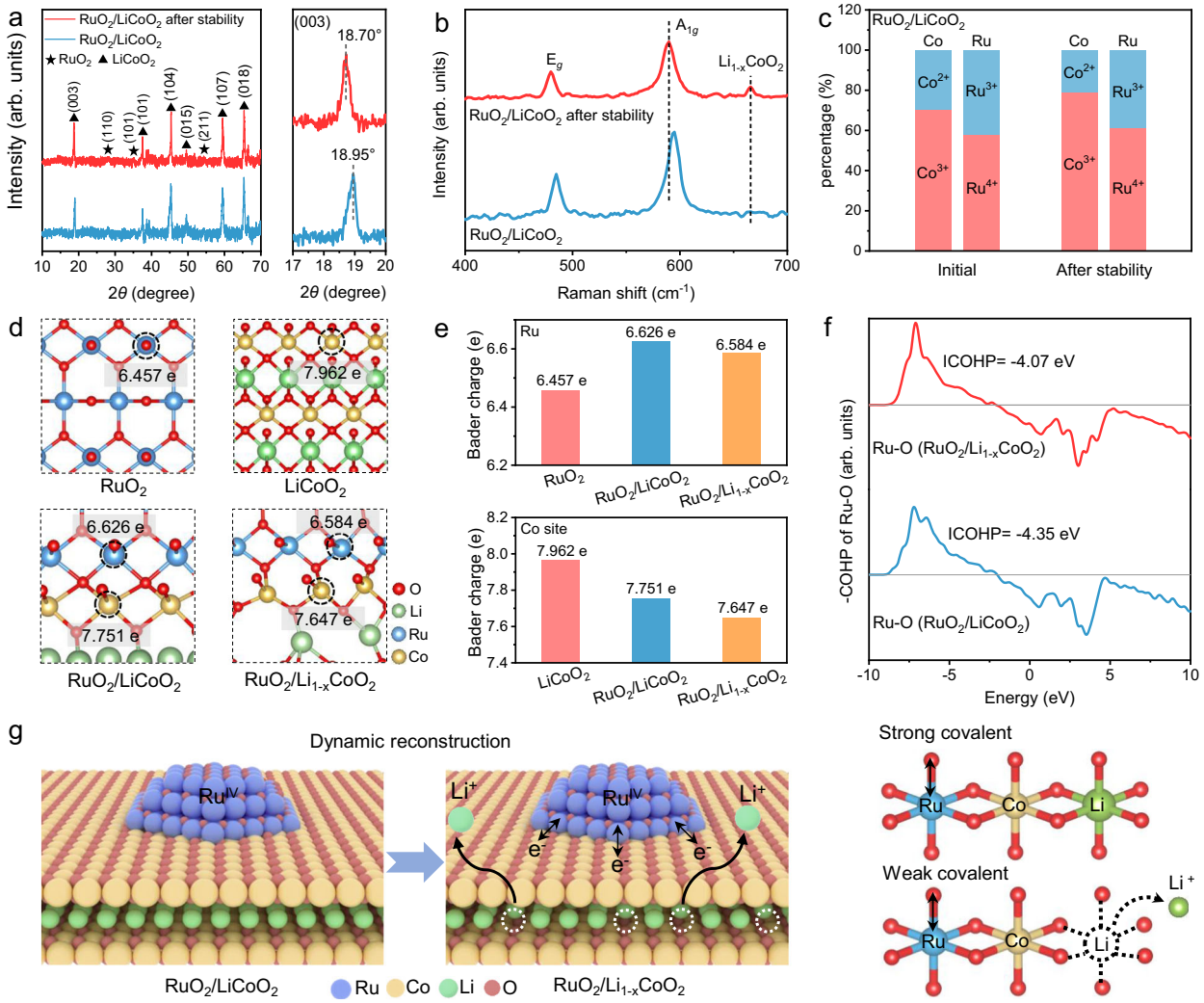

Fig. 4 | Reconstruction of $RuO_2/LiCoO_2$ catalyst after stabilization. a XRD patterns and (**b**) Raman spectra of $RuO_2/LiCoO_2$ and $RuO_2/LiCoO_2$ after stability, respectively. **c** The content of Co^{2+}, Co^{3+}, Ru^{3+}, and Ru^{4+} in $RuO_2/LiCoO_2$ before and after OER stability. **d** Bader charge analysis of RuO_2, $LiCoO_2$, $RuO_2/LiCoO_2$, and $RuO_2/Li_{1-x}CoO_2$, respectively. **e** Comparison of charge amounts of RuO_2, $LiCoO_2$, $RuO_2/LiCoO_2$, and $RuO_2/Li_{1-x}CoO_2$, respectively. **f** COHP of Ru-O in $RuO_2/LiCoO_2$ and $RuO_2/Li_{1-x}CoO_2$, respectively. **g** Schematic diagram of the dynamic evolution of $RuO_2/LiCoO_2$.

voltage of 1.7 V (Supplementary Figs. 59, 60). As a result, the extraction of lithium ions can moderately regulate the electron distribution of $LiCoO_2$ support without destroying the main structure. Remarkably, the valence state of Ru rapidly increases from +4.02 to +5.57 in RuO_2 switching the voltage from OCV to 1.7 V vs. RHE, which is attributed to the excessive oxidation originating from the damage of the RuO_2 structure (Fig. 5h, Supplementary Figs. 61, 62). Based on the above results, the dynamic reconstruction process of $RuO_2/LiCoO_2$ can effectively modify the charge environment of the Ru-O bond and stabilize the lattice oxygen, resulting in improved OER performance.

Origin of high catalytic performance

To investigate the transfer phenomena of reaction intermediates on the electrocatalyst surface, a series of electrochemical measurements are performed. The cyclic voltammetry curves of $RuO_2/LiCoO_2$ and RuO_2 can observe two pairs of redox peaks around 0.5 V and 1.0 V respectively, which correspond to the formation of *OH reaction intermediates with H_2O deprotonation (Fig. 6a). Obviously, the redox peak of $RuO_2/LiCoO_2$ moves downwards than that of RuO_2, indicating favorable H_2O deprotonation and promoting the reaction process[46]. Subsequently, methanol is used as a probe molecule to detect the coverage of *OH intermediates on the catalyst surface (Supplementary Fig. 63). The methanol oxidation reaction (MOR) is more active on OH*-dominated catalyst surfaces due to the mechanism of nucleophilic attack on electrophilic sites[12]. $RuO_2/LiCoO_2$ exhibits high surface OH* coverage compared to RuO_2 in Fig. 6b, implying that $RuO_2/LiCoO_2$ contains more effective OER active sites. Furthermore, the change in catalytic activity of the $RuO_2/LiCoO_2$ catalyst at different pH values is negligible, which is a characteristic of the typical AEM mechanism (Fig. 6c and Supplementary Fig. 64)[47]. In contrast, RuO_2 exhibits a pH-dependent behavior of OER activity, demonstrating the occurrence of an unstable LOM mechanism. The rotating ring-disk electrode test and the adsorption/desorption energy barrier analysis of Li-containing intermediates indicate that it is difficult for the extracted Li ions to participate in the OER process of $RuO_2/LiCoO_2$ (Supplementary Figs. 65–68). Furthermore, $RuO_2/LiCoO_2$ maintains the same potential in electrolytes with different Li-ion concentrations after 50 h of stability testing, further confirming that the small amount of extracted Li has a negligible effect on the performance of the catalyst (Supplementary Fig. 69).

The mechanism of the acidic OER reaction of $RuO_2/LiCoO_2$ and RuO_2 is further monitored by Operando attenuated total reflectance surface-enhanced infrared absorption spectroscopy (ATR-SEIRAS) (Supplementary Fig. 70)[48]. A strong absorption band can be observed in $RuO_2/LiCoO_2$ at about 1033 cm^{-1}, which is identified as O-O

https://doi.org/10.1038/s41467-025-58654-0

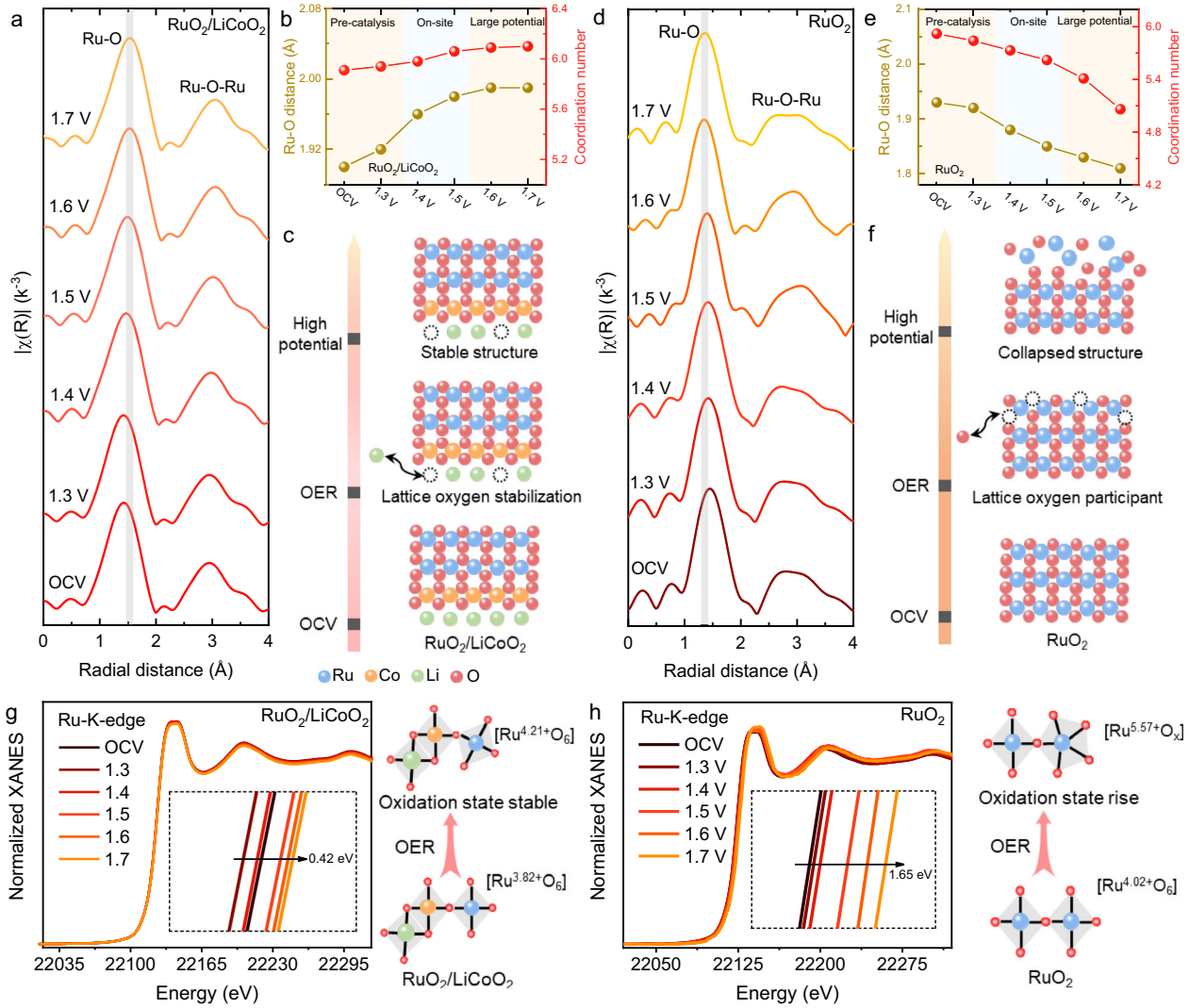

Fig. 5 | In-suit XAS characterization of $RuO_2/LiCoO_2$ confirming the dynamic process. a In situ Ru K-edge EXAFS spectra of $RuO_2/LiCoO_2$ with applied potentials from OCV to 1.7 V. **b** Changes in bond length and intensity of the Ru-O shell of $RuO_2/LiCoO_2$ at different potentials. **c** Schematic diagram of the structural evolution of $RuO_2/LiCoO_2$ at different potentials. **d** In situ Ru K-edge EXAFS spectra of RuO_2 with applied potentials from OCV to 1.7 V. **e** Changes in bond length and intensity of the Ru-O shell of RuO_2 at different potentials. **f** Schematic diagram of the structural evolution of RuO_2 at different potentials. **g** In situ Ru K-edge XANES spectra of $RuO_2/LiCoO_2$. Inset: Oxidation state changes of Ru in $RuO_2/LiCoO_2$. **h** In situ Ru K-edge XANES spectra of RuO_2. Inset: Oxidation state changes of Ru in RuO_2.

stretching in the *OOH intermediate in Fig. 6d[49]. Since *OOH is a typical intermediate of the AEM mechanism, the OER process of $RuO_2/LiCoO_2$ is mainly dominated by AEM. In contrast, the characteristic peaks at 1033 and 1122 cm^{-1} in RuO_2 correspond to *OOH and *OO intermediates, respectively, indicating a combined path of LOM and AEM (Fig. 6e)[50]. Thus, the dynamic reconstruction effect realizes the complete transformation of $RuO_2/LiCoO_2$ electrocatalysis from LOM to AEM mechanism, thereby preventing the dissolution of the catalyst and enhancing OER stability (Fig. 6f). The Gibbs free energy barriers of OER reaction intermediates on the electrocatalyst are calculated to explore the activity differences (Supplementary Figs. 71–73). According to Fig. 6g, the OER rate-determining step (RDS) of $RuO_2/Li_{1-x}CoO_2$, $RuO_2/LiCoO_2$, and RuO_2 is the formation energy barrier of the intermediate *OOH. The $RuO_2/Li_{1-x}CoO_2$ electrocatalyst only requires an energy barrier of 1.77 eV to overcome RDS, which is much lower than that of RuO_2 (2.19 eV). The formation barrier of the *OO intermediate of $RuO_2/Li_{1-x}CoO_2$ is much higher than that of *OOH, which is more conducive to the AEM mechanism (Supplementary Figs. 74–81). In addition, the overlap between Ru d and O p orbitals is reduced, further confirming the weakened covalency of the Ru-O bond. This hinders lattice oxygen from participating in the OER reaction process, thereby enhancing structural stability (Supplementary Figs. 82, 83). As a result, the modification of $Li_{1-x}CoO_2$ support optimizes the binding energy of RuO_2 with key intermediates, resulting in a favorable thermodynamic process and enhanced intrinsic activity.

Discussion

In summary, we have successfully manipulated the bonding environment of RuO_2 during the catalytic reaction by utilizing the dynamic reconstruction of the $LiCoO_2$ support to achieve a balance between activity and stability in acidic OER. Dynamic electrochemical delithiation regulates the electron distribution and coordination structure at the interface, promoting the self-optimization of the $RuO_2/LiCoO_2$ catalyst during the OER process. The weakened covalency of the Ru-O bond triggers a complete transition of the $RuO_2/LiCoO_2$ electrocatalyst from the LOM to the AEM reaction pathway, improving the catalytic stability. As a result, the $RuO_2/LiCoO_2$ electrocatalyst reaches a current density of 10 mA cm^{-2} at a low overpotential of 150 ± 2 mV. In particular, the PEM electrolyzer using $RuO_2/LiCoO_2$ operates stably for 2000 h at a high current density of 1 A cm^{-2}. This work provides a

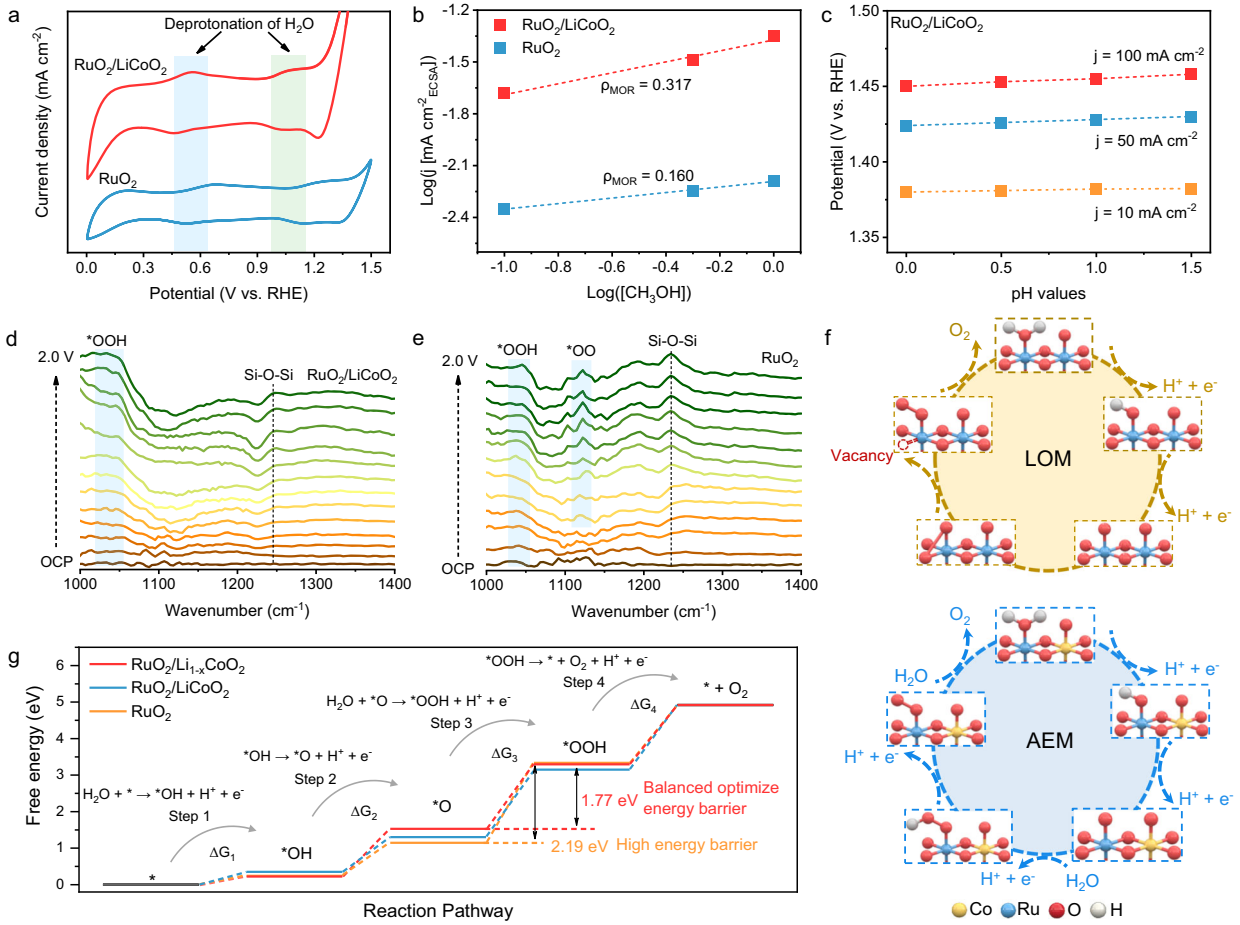

Fig. 6 | Reaction mechanism on $RuO_2/LiCoO_2$. **a** Cyclic voltammetry curves of $RuO_2/LiCoO_2$ and RuO_2 catalysts in 0.5 M H_2SO_4. **b** The function plot between MOR current density and methanol concentration on $RuO_2/LiCoO_2$ and RuO_2 catalysts. **c** The pH dependence of the OER potential at various current densities for $RuO_2/LiCoO_2$ and RuO_2. Operando ATR-SEIRAS spectra of **d** $RuO_2/LiCoO_2$ and **e** RuO_2 at various applied potentials. **f** Schematic diagrams of the OER mechanism on $RuO_2/LiCoO_2$ and RuO_2, respectively. **g** OER Gibbs free energy diagrams of $RuO_2/Li_{1-x}CoO_2$, $RuO_2/LiCoO_2$, and RuO_2, respectively.

method to solve the balance between the activity and stability of ruthenium-based oxide electrocatalysts in acidic OER.

Methods

Experimental section

Materials preparation

Preparation of $LiCoO_2$ Nanosheets. The stoichiometric amount of Co_3O_4 (solid, ACS reagent, ≥ 98%) and 4% excess Li_2CO_3 (solid, ACS reagent, ≥ 98%) was mixed by ball milling for 6 h at 4.47 × *g*. Subsequently, the precursors were calcined for 4 h at 950 °C in air with a heating rate of 5 °C min^{-1} to obtain bulk $LiCoO_2$ powder. The bulk $LiCoO_2$ powders were dispersed in distilled water and sonicated for 4 h in an ice-water bath, maintaining the temperature at 15 °C. The supernatant was collected by centrifugation at 698.75 × *g*. Finally, $LiCoO_2$ nanosheet powders were obtained by freeze-drying the supernatant at −40 °C.

Preparation of $RuO_2/LiCoO_2$. The 50 mg of $LiCoO_2$ and 10 mg of $RuCl_3$ (99.9%) were dissolved in 20 mL of deionized water and magnetically stirred at room temperature for 12 h. Then, the precursor powder was collected by centrifugation at 4025 × *g*. Finally, the obtained powder was calcined in air at 300 °C for 3 h with a heating rate of 5 °C min^{-1} to obtain $RuO_2/LiCoO_2$. For comparison, the amount of $RuCl_3$ was changed to 5 mg and 15 mg to obtain a $RuO_2/LiCoO_2$ electrocatalyst with different RuO_2 loadings.

Characterization. The morphology of the catalysts was characterized by a scanning electron microscope (SEM JEOL JSM-6700F) and transmission electron microscope (TEM FEI Tecnai G2 F20). Aberration-corrected high-angle annular dark-field scanning transmission electron microscope (AC HAADF-STEM) images were taken at JEM-ARM200F equipped with a JED-2300T SDD. X-ray diffraction (XRD) data obtained from Bruker D8 Advance equipment was used to analyze the crystal structure. The elemental compositions were analyzed by ICP (ICP-MS, Inductively coupled plasma-mass spectrometry). X-ray photoelectron spectroscopy (XPS) analysis was performed on an Escalab 250Xi system using Al Kα X-rays. The Co K-edge and Ru K-edge X-ray absorption spectroscopy (XAS) was measured at the beamline of TLS 17C1 and TPS 44A1 at the National Synchrotron Radiation Research Center (NSRRC) in Taiwan.

Electrochemical measurements. The electrochemical performance was tested on an electrochemical workstation using a three-electrode system (Autolab PGSTAT302, Metrohm). Graphite rod and saturated Hg/$HgSO_4$ electrode were used as counter electrode (CE) and reference electrode (RE), respectively. The catalyst, carbon black, and polyvinylidene fluoride (PVDF) were mixed in a weight ratio of 7:2:1, and N-methyl-2-pyrrolidone (NMP) was used as the solvent. The viscous slurry was evenly coated on carbon paper and dried under a vacuum. The catalyst loading is 1 mg_{cat} cm^{-2} and the loading area is 1 cm^2. The measured potential was converted into a reversible hydrogen electrode according to the equation $E_{RHE} = E_{Hg/Hg2SO4} + 0.656\ V + 0.0591\ pH$.

Subsequently, CV was measured at a scan rate of 1 mV s^{-1}. The linear sweep voltammetry (LSV) was performed in N_2-saturated 0.5 M H_2SO_4 solution (pH is 0.3 ± 0.1) at a scan rate of 5 mV s^{-1}. The electrolyte was prepared and used immediately and stored in a glass bottle at room temperature. The potential was corrected according to the $E=E_{applied}$ - iR formula. The electrochemical impedance spectroscopy (EIS) was performed in the frequency range of 0.01-100 kHz with an amplitude of 5 mV. The double-layer capacitance (C_{dl}) was obtained by collecting CV curves with scan rates of 10 to 60 mV s^{-1}. OCP tests were performed with H_2SO_4 saturated with high-purity hydrogen to confirm the reference electrode potential. Calibration experiments were performed at room temperature (25 °C) to reduce temperature effects.

Rotating ring disk electrode (RRDE) test of $RuO_2/LiCoO_2$ catalyst. The 5 mg $RuO_2/LiCoO_2$ catalyst was dispersed in a mixed solution of 980 µL isopropyl alcohol and 20 µL Nafion (5 wt%), followed by ultrasonication for 1 h to obtain a uniformly dispersed catalyst ink. 20 µL of catalyst ink was dropped onto a disk electrode (area 0.2475 cm^2) and dried under vacuum at room temperature to obtain a working electrode. A carbon rod and $Hg/HgSO_4$ were used as the counter electrode and reference electrode, respectively. The linear sweep voltammetry was carried out in 0.5 M H_2SO_4 solution with different Li-ion concentrations at a scan rate of 5 mV s^{-1} and a rotation speed of 1600 rpm.

The electrochemical surface area (ECSA) of an electrocatalyst can be evaluated by electrochemical double capacitance (C_{dl}) according to the following equation:

$$ECSA = \frac{C_{dl}}{C_s} \quad (1)$$

where C_{dl} was determined by taking half the slope of the current differences ($\Delta j = j_{anodic} - j_{cathodic}$) that were plotted as a function of the scan rate in a CV experiment. C_s is the general surface specific capacitance (0.04 mF cm^{-2}).

The turnover frequency (TOF) of the electrocatalyst was calculated by the following equation:

$$TOF = \left(\frac{\text{Formate turnovers per} A_{geo}}{\text{Active sites per} A_{geo}}\right) \quad (2)$$

The formate turnover per geometric area was obtained from the geometric current density for the LSV polarization curves according to the equation:

$$A_{geo} = j_{geo} \times \frac{1\,C\,s^{-1}}{1000\,mA} \times \frac{1\,mol}{96485.3\,C} \times \frac{1}{4} \times \frac{6.023\times10^{23}}{1\,mol\,O_2} \quad (3)$$

Electrochemical in situ ATR-SEIRAS experiments. ATR-SEIRAS measurements were conducted using a Nicolet iS50 FT-IR spectrometer, with each spectrum obtained by accumulating 32 interferograms, achieving a spectral resolution of 8 cm^{-1}. The working electrode preparation involved two key steps. First, an ultra-thin Au film was chemically deposited onto a silicon crystal to enhance infrared signal sensitivity and electron conductivity. Then, a catalyst slurry with a loading of 0.1 mg cm^{-2} was applied onto the Au surface. This slurry was prepared by dispersing 7 mg of catalyst and 3 mg of carbon black in 1 mL ethanol, followed by the addition of 50 µL of Nafion after 30 min of sonication. The assembled working electrodes were placed in a three-electrode electrochemical cell, where $Hg/HgSO_4$ served as the reference electrode, a graphite rod as the counter electrode, and Ar-saturated 0.5 M H_2SO_4 as the electrolyte for the OER reaction[51]. All measurements were performed using linear sweep voltammetry (LSV) to investigate OER reaction intermediates at various applied potentials.

In situ XAFS measurements. In-situ X-ray absorption spectroscopy (XAS), including both XANES and EXAFS at the Ru and Co K-edges, was conducted in total fluorescence yield mode under ambient conditions at BL-12B2 of SPring-8, NSRRC. The measurements were carried out using a custom-designed Teflon container equipped with a Kepton tape-sealed window, allowing X-rays to pass through both the tape and electrolyte. This setup ensured that XAS signals were effectively captured in total fluorescence yield mode at the National Synchrotron Radiation Research Center (NSRRC), SPring-8. The experiments were performed under a three-electrode configuration, consistent with the electrochemical characterization conditions[52]. For data processing, spectral normalization was achieved by removing the pre-edge baseline and adjusting the post-edge region. The k^2-weighted EXAFS oscillations underwent Fourier transformation to facilitate EXAFS analysis, with all EXAFS spectra presented without phase correction. The Fourier-transformed (FT) data fitting was conducted using Artemis (version 0.9.25), employing a k^3 weighting factor with a k-range of 3–12 $Å^{-1}$ and an R-range of 1.0–4.0 Å. The coordination number, bond length, Debye-Waller factor, and energy shift (CN, R, σ^2, and ΔE_0) were determined through fitting without any fixed parameters, while the amplitude reduction factor (S_0^2) was set to 0.85.

PEMWE measurements. $RuO_2/LiCoO_2$ was used as anode catalysts in PEM electrolyzers. Commercial Pt/C was used as a cathode catalyst. The membrane electrode assembly was fabricated via the catalyst-coated membrane technique, covering a geometric area of 2 cm × 2 cm (4 cm^2). The catalyst powder was dispersed in isopropanol, deionized water, and Nafion solution to prepare the ink. The uniformly dispersed ink was obtained by slice emulsification and ultrasonic cell disruption. The well-dispersed $RuO_2/LiCoO_2$ and Pt/C catalyst inks were sprayed on both sides of the PEM, respectively. The loadings of $RuO_2/LiCoO_2$ anode and Pt/C cathode are 4 mg_{cat} cm^{-2} and 1 mg_{cat} cm^{-2}, respectively. Nafion 115 was used as a proton exchange membrane (PEM) and was treated with H_2O_2 and 0.5 M H_2SO_4 at 80 °C for 1 h in sequence. The size of the proton exchange membrane was 2.6 cm^2 and the membrane thickness was 127 µm. The sprayed membrane, anode gas diffusion layer (Ti felt), and cathode gas diffusion layer (carbon paper) were hot-pressed at 130 °C and 10 MPa pressure to obtain a membrane electrode assembly. Subsequently, a PEM water electrolyzer was assembled and tested at 80 °C using pure water as the electrolyte. The polarization curve of PEMWE was obtained at a scan rate of 5 mV s^{-1}, and a chronopotentiometric test was performed at 1 A cm^{-2} to evaluate the stability.

DFT calculations. All density functional theory (DFT) calculations were conducted using the Vienna Ab initio Simulation Package (VASP)[53]. The projector augmented wave (PAW) pseudopotential was applied in combination with the PBE generalized gradient approximation (GGA) exchange-correlation functional[54]. To appropriately describe the localized d-electrons of Co, the DFT + U method was employed, incorporating a Hubbard-U correction of Ueff(Co) = 3.32 eV, determined via linear response theory. The calculations were performed with a plane wave basis set energy cutoff of 500 eV, and a Monkhorst-Pack k-point grid of 3 × 3 × 1 was used for Brillouin zone sampling. Spin polarization was considered, and full structural relaxation was conducted until the energy convergence criterion reached 10^{-5} eV per atom, with the final force acting on each atom kept below 0.05 eV $Å^{-1}$. Additionally, Pourbaix diagrams were generated using the Atomic Simulation Environment (ASE), where input formation energies were derived from DFT calculations of bulk and surface models[55].

The adsorption energy of reaction intermediates can be computed using the following Equation:

$$\Delta G_{ads} = E_{ads} - E_* + \Delta E_{ZPE} - T\Delta S \quad (4)$$

Where ads = OH*, O*, OOH*, an $E_{ads} - E_*$ is the binding energy, ΔE_{ZPE} is the zero-point energy change, ΔS is the entropy change. In this work,

the values of ΔE_{ZPE} and ΔS were obtained by vibration frequency calculation.

The Gibbs free energy of the reaction steps can be calculated by the following four Equations:

$$H_2O + {}^* \leftrightarrow HO^* + H^+ + e^- \quad (5)$$

$$\Delta G_1 = \Delta G_{HO^*} + G_H - \Delta G_* - G_{H_2O} - eU \quad (6)$$

$$HO^* \leftrightarrow O^* + H^+ + e^- \quad (7)$$

$$\Delta G_2 = \Delta G_{O^*} - \Delta G_{HO^*} + G_H - eU \quad (8)$$

$$O^* + H_2O \leftrightarrow OOH^* + H^+ + e^- \quad (9)$$

$$\Delta G_3 = \Delta G_{OOH^*} + G_H - \Delta G_{O^*} - G_{H_2O} - eU \quad (10)$$

$$OOH^* \leftrightarrow {}^* + O_2 + H^+ + e^- \quad (11)$$

$$\Delta G_4 = \Delta G_* - \Delta G_{OOH^*} + G_H + G_{O_2} - eU \quad (12)$$

In this work, ΔG_{1-4} were calculated at U = 0.

Data availability

The source data underlying Figures are provided as a Source Data file. Source data are provided with this paper.

References

1. Li, A. et al. Atomically dispersed hexavalent iridium oxide from MnO_2 reduction for oxygen evolution catalysis. *Science* **384**, 666–670 (2024).
2. Wu, Z.-Y. et al. Non-iridium-based electrocatalyst for durable acidic oxygen evolution reaction in proton exchange membrane water electrolysis. *Nat. Mater.* **22**, 100–108 (2023).
3. Wang, L. et al. Optimizing edge active sites via intrinsic in-plane iridium deficiency in layered iridium oxides for oxygen evolution electrocatalysis. *Adv. Mater.* **36**, 2312608 (2024).
4. Qin, Y. et al. RuO_2 electronic structure and lattice strain dual engineering for enhanced acidic oxygen evolution reaction performance. *Nat. Commun.* **13**, 3784 (2022).
5. Zhu, J. et al. Regulative electronic states around ruthenium/ruthenium disulphide heterointerfaces for efficient water splitting in acidic media. *Angew. Chem. Int. Ed.* **60**, 12328–12334 (2021).
6. Song, H. et al. RuO_2–CeO_2 lattice matching strategy enables robust water oxidation electrocatalysis in acidic media via two distinct oxygen evolution mechanisms. *ACS Catal.* **14**, 3298–3307 (2024).
7. Jin, H. et al. Dynamic rhenium dopant boosts ruthenium oxide for durable oxygen evolution. *Nat. Commun.* **14**, 354 (2023).
8. Deng, L. et al. Valence oscillation of Ru active sites for efficient and robust acidic water oxidation. *Adv. Mater.* **35**, 2305939 (2023).
9. Lee, K. et al. Modulating the valence electronic structure using earth-abundant aluminum for high-performance acidic oxygen evolution reaction. *Chem.* **9**, 3600–3612 (2023).
10. Chen, D. et al. Heteroanion induced structural asymmetricity centered on Ru sites switches the rate-determining step of acid water oxidation. *Energy Environ. Sci.* **17**, 1885–1893 (2024).
11. Xi, W. et al. Accelerating Ru^0/Ru^{4+} adjacent dual sites construction by copper switch for efficient alkaline hydrogen evolution. *Adv. Energy Mater.* **13**, 2302668 (2023).
12. Li, L. et al. Lanthanide-regulating Ru-O covalency optimizes acidic oxygen evolution electrocatalysis. *Nat. Commun.* **15**, 4974 (2024).
13. Xu, Y. et al. Strain-modulated Ru-O covalency in Ru-Sn oxide enabling efficient and stable water oxidation in acidic solution. *Angew. Chem. Int Ed. Engl.* **63**, e202316029 (2024).
14. Liang, X. et al. Electrocatalytic water oxidation activity-stability maps for perovskite oxides containing 3d, 4d and 5d transition metals. *Angew. Chem. Int. Ed.* **62**, e202311606 (2023).
15. Qin, Y. et al. Orthorhombic $(Ru, Mn)_2O_3$: a superior electrocatalyst for acidic oxygen evolution reaction. *Nano Energy* **115**, 108727 (2023).
16. Xiao, K., Wang, Y., Wu, P., Hou, L. & Liu, Z.-Q. Activating lattice oxygen in spinel $ZnCo_2O_4$ through filling oxygen vacancies with fluorine for electrocatalytic oxygen evolution. *Angew. Chem. Int. Ed.* **62**, e202301408 (2023).
17. Lee, G. R. et al. Efficient and sustainable water electrolysis achieved by excess electron reservoir enabling charge replenishment to catalysts. *Nat. Commun.* **14**, 5402 (2023).
18. Long, X. et al. Ru-RuO_2 nano-heterostructures stabilized by the sacrificing oxidation strategy of Mn_3O_4 substrate for boosting acidic oxygen evolution reaction. *Appl. Catal. B Environ.* **343**, 123559 (2024).
19. Du, K. et al. Interface engineering breaks both stability and activity limits of RuO_2 for sustainable water oxidation. *Nat. Commun.* **13**, 5448 (2022).
20. Jia, H., Yao, N., Yu, C., Cong, H. & Luo, W. Unveiling the electrolyte cations dependent kinetics on CoOOH-catalyzed oxygen evolution reaction. *Angew. Chem. Int. Ed.* **62**, e202313886 (2023).
21. Sun, Y. et al. Navigating surface reconstruction of spinel oxides for electrochemical water oxidation. *Nat. Commun.* **14**, 2467 (2023).
22. Zheng, X. et al. Ru–Co pair sites catalyst boosts the energetics for the oxygen evolution reaction. *Angew. Chem. Int. Ed.* **61**, e202205946 (2022).
23. Wang, J. et al. Redirecting dynamic surface restructuring of a layered transition metal oxide catalyst for superior water oxidation. *Nat. Catal.* **4**, 212–222 (2021).
24. Hu, E. et al. Oxygen-redox reactions in $LiCoO_2$ cathode without O–O bonding during charge-discharge. *Joule* **5**, 720–736 (2021).
25. Zheng, X. et al. Enriched d-band holes enabling fast oxygen evolution kinetics on atomic-layered defect-rich lithium cobalt oxide nanosheets. *Adv. Funct. Mater.* **32**, 2200663 (2022).
26. Zheng, X. et al. Electronic structure engineering of $LiCoO_2$ toward enhanced oxygen electrocatalysis. *Adv. Energy Mater.* **9**, 1803482 (2019).
27. Zheng, X. et al. Multifunctional active-center-transferable platinum/lithium cobalt oxide heterostructured electrocatalysts towards superior water splitting. *Angew. Chem. Int. Ed.* **59**, 14533–14540 (2020).
28. Yan, G. et al. Ultrathin two-dimensional medium-entropy oxide as a highly efficient and stable electrocatalyst for oxygen evolution reaction. *Nano Res* **17**, 2555–2562 (2024).
29. Zhu, W. et al. Stable and oxidative charged Ru enhance the acidic oxygen evolution reaction activity in two-dimensional ruthenium-iridium oxide. *Nat. Commun.* **14**, 5365 (2023).
30. Ping, X. et al. Locking the lattice oxygen in RuO(2) to stabilize highly active Ru sites in acidic water oxidation. *Nat. Commun.* **15**, 2501 (2024).
31. Yao, N. et al. Atomically dispersed Ru oxide catalyst with lattice oxygen participation for efficient acidic water oxidation. *Chem.* **9**, 1882–1896 (2023).
32. Deng, L. et al. Activity-stability balance: the role of electron supply effect of support in acidic oxygen evolution. *Small* **19**, e2302238 (2023).
33. Zhang, X.-L. et al. Efficient acidic hydrogen evolution in proton exchange membrane electrolyzers over a sulfur-doped marcasite-type electrocatalyst. *Sci. Adv.* **9**, eadh2885 (2023).
34. Rao, P. et al. Single atomic cobalt electrocatalyst for efficient oxygen reduction reaction. *eScience* **2**, 399–404 (2022).

35. Dan, M. et al. Dual-axial engineering on atomically dispersed catalysts for ultrastable oxygen reduction in acidic and alkaline solutions. *Proc. Natl Acad. Sci. USA* **121**, e2318174121 (2024).
36. Jian, L., Wang, G., Liu, X. & Ma, H. Unveiling an S-scheme F–Co_3O_4@Bi_2WO_6 heterojunction for robust water purification. *eScience* **4**, 100206 (2024).
37. Wang, Z. et al. Optimizing the oxygen-catalytic performance of Zn–Mn–Co spinel by regulating the bond competition at octahedral sites. *Adv. Funct. Mater.* **33**, 2214275 (2023).
38. Sun, K. et al. Manipulating the spin state of Co sites in metal–organic frameworks for boosting CO_2 photoreduction. *J. Am. Chem. Soc.* **146**, 3241–3249 (2024).
39. Yang, F. et al. Sub-3 nm Pt@Ru toward outstanding hydrogen oxidation reaction performance in alkaline media. *J. Am. Chem. Soc.* **145**, 27500–27511 (2023).
40. Tian, X. et al. Synergy of dendrites-impeded atomic clusters dissociation and side reactions suppressed inert interface protection for ultrastable Zn anode. *Adv. Mater.* **36**, 2400237 (2024).
41. Sun, Z. et al. Lattice strain and mott–schottky effect of the charge-asymmetry Pd_1Fe single-atom alloy catalyst for semi-hydrogenation of alkynes with high efficiency. *ACS Nano* **18**, 13286–13297 (2024).
42. Yu, Z.-Y. et al. General synthesis of tube-like nanostructured perovskite oxides with tunable transition metal–oxygen covalency for efficient water electrooxidation in neutral media. *J. Am. Chem. Soc.* **144**, 13163–13173 (2022).
43. Kuang, J., Deng, B., Jiang, Z., Wang, Y. & Jiang, Z.-J. Sr-stabilized $IrMnO_2$ solid solution nano-electrocatalysts with superior activity and excellent durability for oxygen evolution reaction in acid Media. *Adv. Mater.* **36**, 2306934 (2024).
44. Shi, Z. et al. Customized reaction route for ruthenium oxide towards stabilized water oxidation in high-performance PEM electrolyzers. *Nat. Commun.* **14**, 843 (2023).
45. Wei, Y. et al. Triggered lattice-oxygen oxidation with active-site generation and self-termination of surface reconstruction during water oxidation. *Proc. Natl Acad. Sci. USA* **120**, e2312224120 (2023).
46. Hao, Y. et al. Switching the oxygen evolution mechanism on atomically dispersed Ru for enhanced acidic reaction kinetics. *J. Am. Chem. Soc.* **145**, 23659–23669 (2023).
47. Rong, C. et al. Defect-balanced active and stable Co_3O_{4-x} for proton exchange membrane water electrolysis at ampere-level current density. *Energy Environ. Sci.* **17**, 4196–4204 (2024).
48. Delmo, E. P. et al. In situ infrared spectroscopic evidence of enhanced electrochemical CO_2 reduction and C–C coupling on oxide-derived copper. *J. Am. Chem. Soc.* **146**, 1935–1945 (2024).
49. Lin, Y. et al. In situ identification and time-resolved observation of the interfacial state and reactive intermediates on a cobalt oxide nanocatalyst for the oxygen evolution reaction. *ACS Catal.* **12**, 5345–5355 (2022).
50. Zhang, T. et al. Spatial configuration of Fe–Co dual-sites boosting catalytic intermediates coupling toward oxygen evolution reaction. *Proc. Natl Acad. Sci. USA* **121**, e2317247121 (2024).
51. Hao, Y. et al. Designing neighboring-site activation of single atom via tunnel ions for boosting acidic oxygen evolution. *Nat. Commun.* **15**, 8015 (2024).
52. Hung, S.-F. et al. Unraveling geometrical site confinement in highly efficient iron-doped electrocatalysts toward oxygen evolution reaction. *Adv. Energy Mater.* **8**, 1701686 (2018).
53. Kresse, G. & Furthmüller, J. Efficient iterative schemes for ab initio total-energy calculations using a plane-wave basis set. *Phys. Rev. B* **54**, 11169–11186 (1996).
54. Blöchl, P. E. Projector augmented-wave method. *Phys. Rev. B* **50**, 17953–17979 (1994).
55. Hjorth Larsen, A. et al. The atomic simulation environment—a Python library for working with atoms. *J. Phys.: Condens. Matter* **29**, 273002 (2017).

Acknowledgements

This work was supported by the National Natural Science Foundation of China (52371226, L.L.L and 52371226, S.J.P), and the Scientific and Technological Innovation Special Fund for Carbon Peak and Carbon Neutrality of Jiangsu Province (BK20220039, S.J.P). This work was also supported by the 2030 Cross-Generation Young Scholars Program of the National Science and Technology Council in Taiwan under the grant NSTC 112-2628-E-007-014-MY4 to Dr. Han Yi-Chen. The authors thank the National Synchrotron Radiation Research Center, Hsinchu, Taiwan, for providing synchrotron XAS beamline TLS 17C1 and TPS 44A1.

Author contributions

L.W., S.Z., L.L., F.H. and S.P. designed the study. L.W. and S.P. conducted the experiments. L.W., S.F.H., J.J.M., C.Z., Y.Z., T.Y.C. and H.Y.C. participated in the characterization of the samples. L.W., Y.W., S.B., S.L., Y.W. and S.P. analyzed data. L.W. wrote the paper. S. P. conceived the idea and revised the manuscript.

Competing interests

The authors declare no competing interests.

Additional information

Supplementary information The online version contains supplementary material available at https://doi.org/10.1038/s41467-025-58654-0.

Correspondence and requests for materials should be addressed to Linlin Li, Feng Hu or Shengjie Peng.

Peer review information *Nature Communications* thanks Sung Jong Yoo, Ronghui Qi and the other, anonymous, reviewer(s) for their contribution to the peer review of this work. A peer review file is available.